KSCE Journal of Civil Engineering
DOI 10.1007/s12205-023-0229-3

pISSN 1226-7988, eISSN 1976-3808
www.springer.com/12205

Structural Engineering

Prediction of the Moment Capacity of FRP-Strengthened RC Beams Exposed to Fire Using ANNs

Seong-Muk Kang[a] **and Jin-Kook Kim**[a]

[a]*Member, Dept. of Civil Engineering, Seoul National University of Science and Technology, Seoul 01811, Korea*

ARTICLE HISTORY

Received 5 December 2022
Revised 26 March 2023
Accepted 8 May 2023
Published Online 24 June 2023

KEYWORDS

ANN model
FRP-strengthened RC beam
Heat transfer analysis
Hyperparameters
Moment capacity
Section equilibrium method

ABSTRACT

In this study, an Artificial Neural Network (ANN) model to predict the moment capacity of Fiber Reinforced Plastic (FRP) strengthened Reinforced Concrete (RC) beams exposed to fire is developed. The software ABAQUS heat transfer analysis is verified by comparison with the fire resistance test results. Through this heat transfer analysis, the temperature distribution of the beam section is determined, and 400 datasets are obtained using the moment capacity calculation method combined with the section equilibrium method. The data consist of eight input parameters: the beam width, beam height, FRP area, rebar area, concrete compressive strength, insulation thickness, concrete cover depth, and fire exposure time. The output parameter is the moment capacity. The ANN model is developed through a sensitivity study using the algorithm type and the number of hidden-layer neurons as variables. The average error between the predicted data of the developed ANN model and the target data obtained from the moment capacity calculation method was 0.35 kN·m, and the average relative error was 0.2512%, showing high accuracy. Therefore, the ANN model developed here can determine the moment capacity without complex calculations. The effects of the input parameters on the moment capacity of the FRP-strengthened RC beams exposed to fire are investigated using the ANN model.

1. Introduction

Recently, FRP has been increasingly used for the repair, restoration, and reinforcement of RC structural members due to various advantages, such as its high strength, durability, and abrasion resistance. However, FRP-strengthened RC structural members have poor fire resistance, unlike general RC structural members, meaning that they are vulnerable to fire (Bakis et al., 2002; Ahmed and Kodur, 2011a; Ahmed and Kodur 2011b; Kodur and Bhatt, 2018).

FRP composite laminate materials are composed of FRP fibers, capable of withstanding high temperatures, and a resin matrix with a low glass-transition temperature. An FRP composite laminate starts to deteriorate as the resin matrix softens at the glass-transition temperature and loses its bonding ability at the decomposition temperature, resulting in a sharp deterioration in the mechanical properties. This is especially likely when the laminate material is exposed to fire. In addition, in such events, the temperature of the adhesive between the FRP and concrete increases. When the temperature of the adhesive reaches its glass-transition temperature, the mechanical properties of the adhesive are reduced, leading again to FRP debonding. For these reasons, FRP-strengthened RC structural members should include insulation (Ahmed and Kodur, 2011a; Kodur and Bhatt, 2018).

It is crucial to predict the moment capacity of FRP-strengthened RC beams (FSRBs) containing an insulating material upon exposure to fire. A fire causes high temperatures in the FSRB even with insulation, which greatly degrades the mechanical properties, as mentioned above. Complex calculations cannot be avoided when calculating the moment capacity of a FSRB with insulation. First, the tensile and compressive forces must be obtained using the fire exposure time, the dimensions of the cross-section, whether FRP debonding occurs, and the strength of the material. Then, the moment capacity is calculated using the equilibrium of the tensile and compressive forces (Xiang and Wang, 2013). An ANN can predict the moment capacity without these complex calculations.

ANNs are used by many researchers in the field of structural

CORRESPONDENCE Jin-Kook Kim jinkook.kim@seoultech.ac.kr Dept. of Civil Engineering, Seoul National University of Science and Technology, Seoul 01811, Korea

ⓒ 2023 Korean Society of Civil Engineers

engineering. Bengar et al. (2016) predicted the curvature value by developing an ANN model, finding it to be complicated to calculate the exact curvature value of a RC beam. Erdem (2010) developed an ANN model that predicts the moment capacity of an RC beam upon exposure to fire and found that it was possible to predict the moment capacity accurately after a fire given a certain range of input parameters. Cai et al. (2019) developed and validated a model for calculating the residual shear of RC beams after a fire using an ANN. Their model was used to investigate the effects of certain input parameters on the shear resistance of the beam. Naser et al. (2012) developed a model that predicts the temperature distribution of RC T-beams reinforced with CFRP plates under a fire load using an ANN.

While many researchers have used ANNs in structural engineering, a study to predict the moment capacity of FSRBs exposed to fire using an ANN has not yet been conducted.

In this study, A new approach is proposed to predict the moment capacity of FSRBs exposed to fire using ANN. Unlike traditional methods that require complex calculations to determine the tensile and compressive forces and the moment capacity of the FSRB, the ANN model can predict the moment capacity without such calculations. This study contributes to the field of structural engineering by introducing a new method for predicting the moment capacity of FSRBs exposed to fire, which can be applied to design fire-resistant structures using FRP-strengthened RC members.

2. Heat Transfer Analysis

2.1 Heat Transfer Analysis Theory

Heat transfer refers to thermal energy that is transferred due to a temperature difference between different media. Heat is transferred in three ways: conduction, convection, and radiation (Bergman et al., 2011).

Conduction refers to energy transferred from a high-energy particle to a low-energy particle by interaction between the particles, and it can be calculated as

$$q'' = k\frac{\Delta T}{L}, \tag{1}$$

where q'' is the heat rate by conduction (W/m^2), k is the thermal conductivity (W/m·k), ΔT is the temperature difference (K), and L is the thickness (m).

Convection is the transfer of heat between a surface and a flowing liquid or gas adjacent to it. It can be calculated as

$$q'' = h(T_s - T_\infty), \tag{2}$$

where q'' is the convective heat flux (W/m^2), h is the convection heat transfer coefficient (W/m^2·k), T_s is the surface temperature (K), and T_∞ is the fluid temperature at a sufficient distance from the surface (K).

Radiation is the transfer of energy emitted in the form of electromagnetic waves from the surface of a material; it can be calculated as.

$$q'' = \varepsilon\sigma(T_s^4 - T_{sur}^4), \tag{3}$$

where q'' is the surface emissive power (W/m^2), ε is the emissivity, σ is the Boltzmann constant (5.67×10^{-8} W/m^{2}K^4), and T_s is the absolute temperature (K).

2.2 FEM Analysis Modeling

To obtain the moment capacity of the FSRB exposed to fire, first it is important to obtain the temperature distribution of the beam through a verified heat transfer analysis. In this study, the heat transfer analysis of FSRBs exposed to fire was verified by comparing the outcome with the cross-sectional temperature change from a fire resistance test and a heat transfer analysis by Ahmed et al. (2011b). The heat transfer analysis was simulated using the general-purpose software program ABAQUS (2010). The cross-sectional dimensions, lengths, and positions of the thermocouples (TC5, TC6, TC9, F/C) of the beam are shown in Figs. 1(a) – 1(c). Concrete, FRP and insulation were modeled as solid materials and were simulated using the heat transfer element DC3D8. The rebar was modeled as a wire and was simulated with the heat transfer element DC1D2. The thermal properties of the concrete and rebar followed the material model of Eurocode 4 (2005) (Figs. 2). The thermal properties of the FRP were referenced from the material model of Bisby (2003), and the thermal properties of the insulation were sourced from the material model used for the heat transfer analysis by Ahmed et al. (2011b) (Figs. 2). In the heat transfer analysis, both the FRP and the rebar were modeled as fully bonded to the concrete by the verified modeling of Hawileh et al. (2009) and Panahi et al (2021). Afterwards, when calculating the structure to obtain moment capacity, if the temperature of the FRP exceeds the temperature of the glass-transition of adhesive, the FRP bond line is considered completely damaged and that FRP element is debonded. Also, it should be noted that this heat transfer analysis model does not take into account the debonding or cracking of the insulation in the analysis by Ahmed et al. (2011b). As a convective boundary condition, the values recommended in Eurocode 4 (2005), 25 W/m^2K and 9 W/m^2K, were applied for the convective heat transfer coefficient for the fire-exposed and non-fire-exposed surfaces, respectively. As shown in Fig. 1(d), the surfaces exposed to fire have three sides excluding the top side of the beam. Emissivity of 0.12 and a Boltzmann constant of 5.67×10^{-8} W/m$^2K^4$ were applied as the radiation boundary conditions. The heating temperature of the fire-exposed surface of the beam followed the standard fire curve from the ASTM E 119-11 (2010) specification.

2.3 Validation of the Heat Transfer Analysis

The validity of the heat transfer analysis model (Kang_FEM) by ABAQUS is secured by comparing the fire resistance test results (Ahmed_Test) and the heat transfer analysis results (Ahmed_FEM) in Ahmed et al. (2011b). Fig. 3(a) shows the mesh size and temperature distribution of the beam cross-section in what is a heat transfer analysis model (Kang_FEM). In addition, the figure shows the temperature distribution of the tension rebar, compression

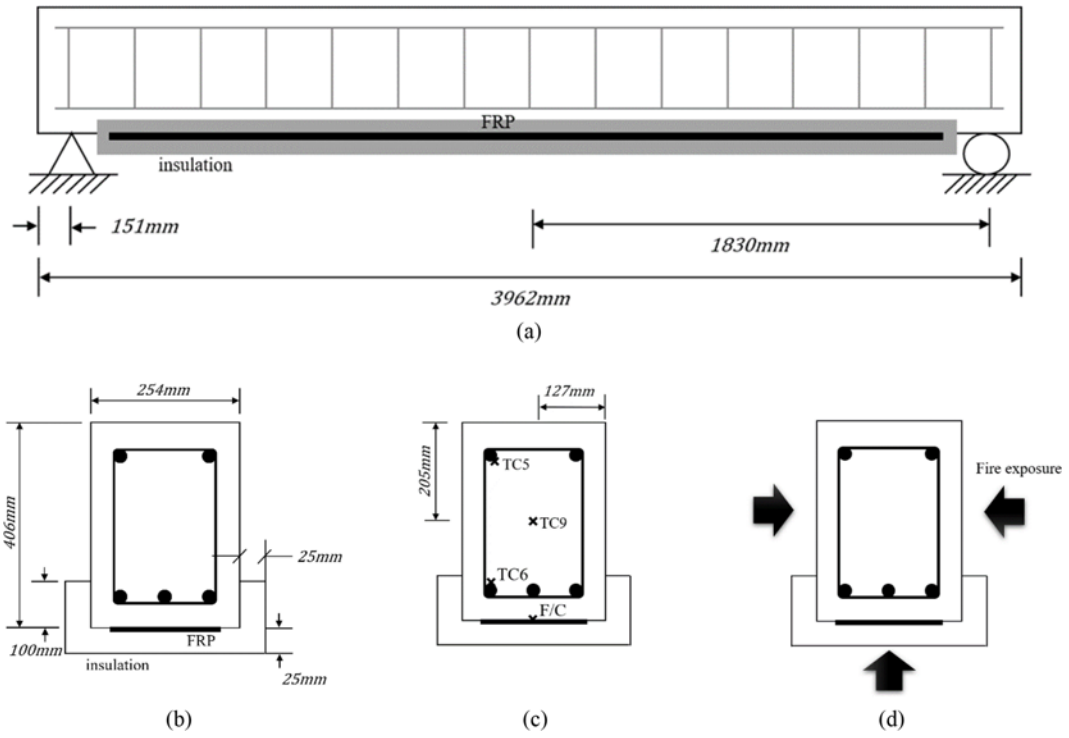

Fig. 1. Details of the FSRB: (a) Elevation, (b) Beam Cross-Section, (c) Thermocouple Position, (d) Boundary Condition

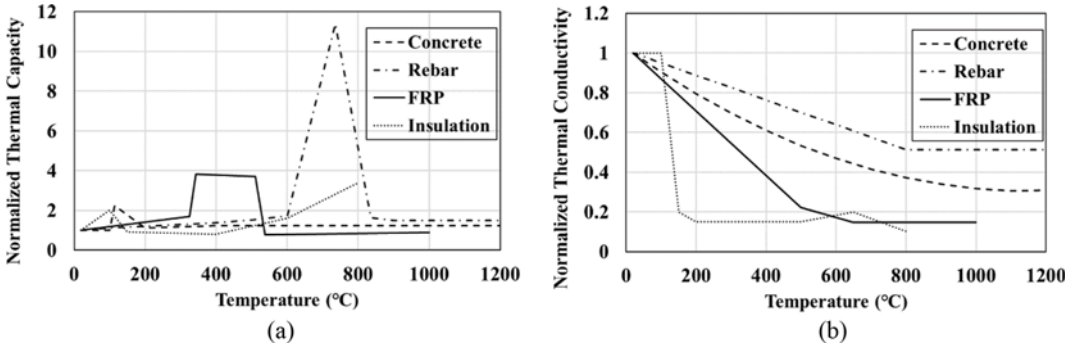

Fig. 2. Thermal Properties of the Material: (a) Normalized Thermal Capacity, (b) Normalized Thermal Conductivity

rebar and stirrup.

Figure 3(b) compares the temperature at the interface between the FRP and concrete (F/C) and the tensile rebar (TC6), and Fig. 3(c) compares the temperature at the intermediate depth of a concrete section (TC9) and a compression rebar (TC5). Throughout the fire, the temperature distribution at all points except that in the test results of the interface (F/C) between the FRP and concrete appears to be consistent. In the test of the interface (F/C) between the FRP and concrete, some of the insulation became detached due to FRP peeling at 38 minutes, which is not consistent with the analysis results. The heat transfer analysis model cannot explain this detached insulation (Ahmed et al., 2011b). In other situations apart from these, the heat transfer analysis model (Kang_FEM) indicates that the overall temperature distribution upon exposure to fire is accurate and effective. Therefore, the validity of the heat transfer analysis of a FSRB exposed to fire is secured.

3. Determination of the Moment Capacity of a FSRB Exposed to Fire

To calculate the moment capacity of a FSRB exposed to fire, the temperature distribution must be determined by a heat transfer analysis. It is therefore necessary to determine the strength of the material and whether the FRP is debonded and to calculate the tensile and compressive forces of the beam cross-section. The moment capacity calculated when the tensile and compressive forces are equal is the moment capacity of the FSRB exposed to fire. The procedure for calculating the moment capacity of a FSRB exposed to fire is shown in the flowchart in Fig. 4.

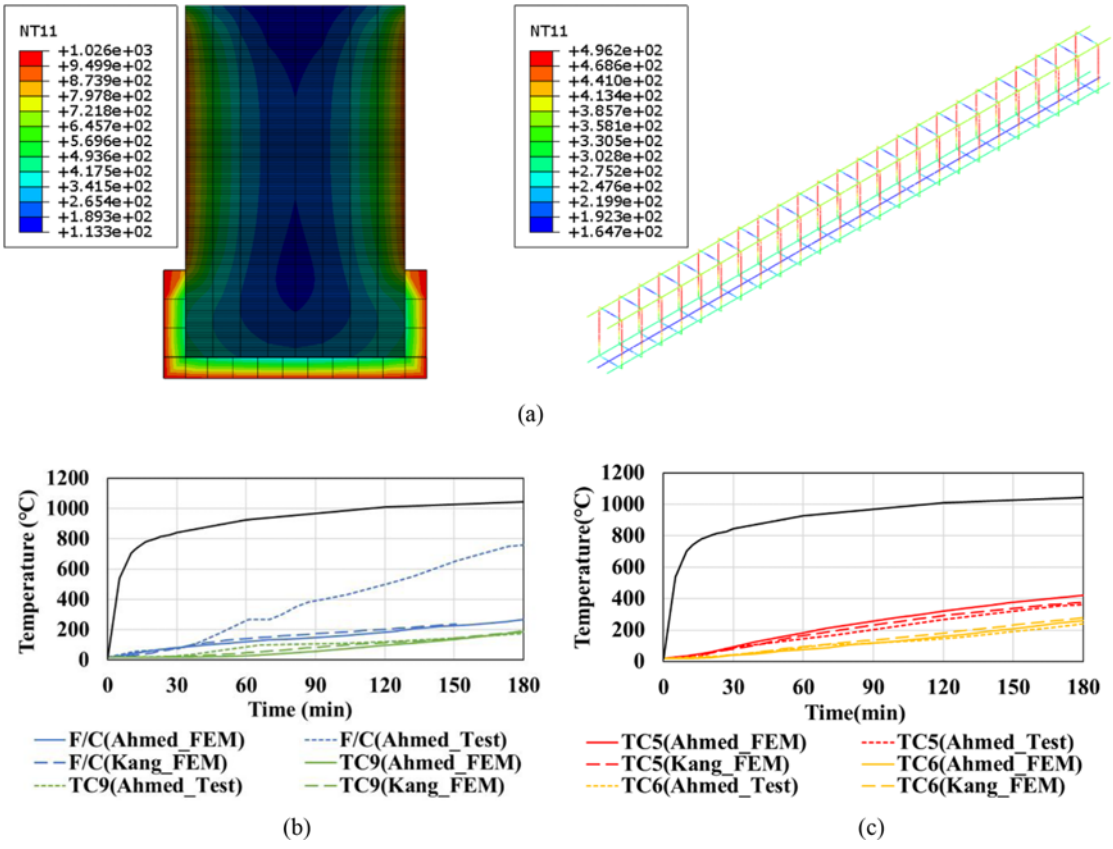

Fig. 3. FEM Analysis Results and Temperature Comparisons: (a) Temperature Distribution of the Cross-Section and Reinforcement, (b) F/C and TC9, (C) TC5 and TC6

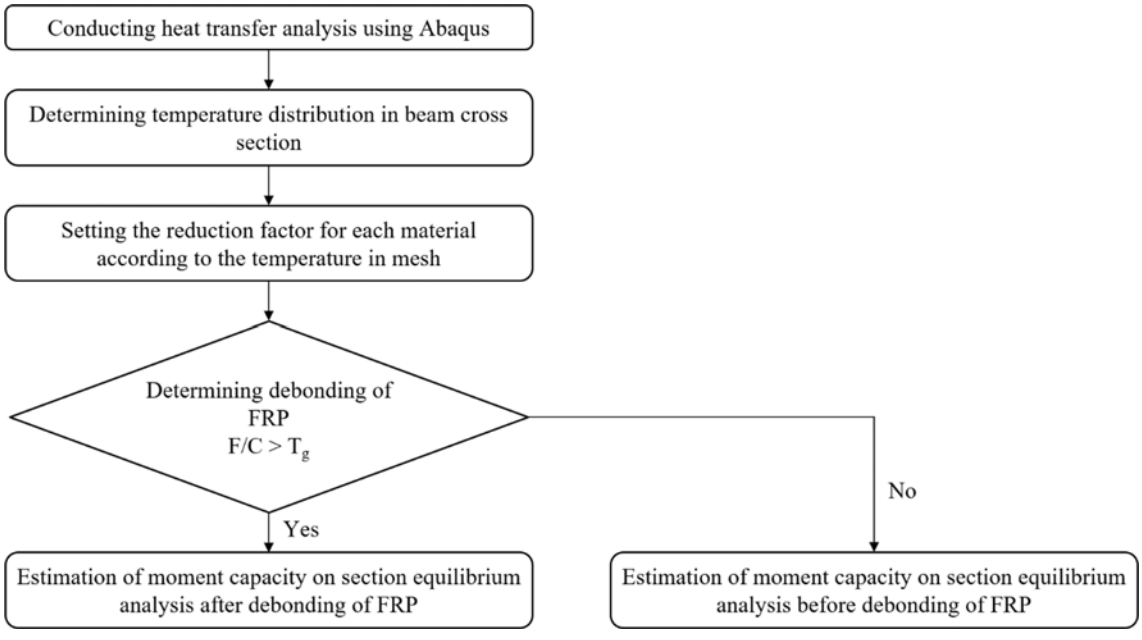

Fig. 4. Procedure for Calculating the Moment Capacity

3.1 Material Properties According to the Temperature

As the temperature increases, the reduction in the compressive strength of the concrete must be considered. The compressive strength reduction factor of concrete can be obtained by the formula provided by Eurocode 2 (2004).

$$\frac{f_{ck,T}}{f_{ck,20°C}} = k_c$$

$$\begin{aligned} k_c &= 1 && 0 \le T \le 100 \\ k_c &= 1.067 - 0.00067T && 100 \le T \le 400 \\ k_c &= 1.44 - 0.0016T && 400 \le T \le 900 \\ k_c &= 0 && 900 \le T \end{aligned} \quad (4)$$

Here, $f_{ck,T}$ and $f_{ck,20°C}$ are the concrete compressive strength at temperature T and the concrete compressive strength at 20 °C. k_c is the compressive strength reduction factor of concrete according to the temperature.

The decrease in the tensile strength of the rebar with an increase in the temperature must be taken into account, as with the concrete. The tensile strength reduction factor of rebar can be obtained by the formula provided by Eurocode 2 (2004).

$$\frac{f_{s,T}}{f_{s,20°C}} = k_s$$

$$\begin{aligned} k_s &= 1 && 0 \le T \le 350 \\ k_s &= 1.899 - 0.00257T && 350 \le T \le 700 \\ k_s &= 0.24 - 0.0002T && 700 \le T \le 1200 \\ k_s &= 0 && 1200 \le T \end{aligned} \quad (5)$$

Here, $f_{s,T}$ and $f_{s,20°C}$ are the tensile strength of the rebar at temperature T and the tensile strength of the rebar at 20 °C. k_s is the tensile strength reduction factor of rebar according to the temperature.

FRP does not undergo plastic deformation, and brittle fractures occur. Therefore, when calculating the moment capacity through a cross-sectional equilibrium analysis, the FRP strain of the elastically deformed part is taken into account. Unlike concrete or rebar, FRP must take into account the elastic modulus reduction factor as the temperature increases. The elastic modulus reduction factor of FRP according to the temperature can be obtained by the formula provided by Bisby (2003).

$$\frac{E_{frp,T}}{E_{frp,20°C}} = k_{frp,E}$$

$$k_{frp,E} = \frac{1-0.05}{2}\tanh[-0.00868*(T-367.41)] + \frac{1+0.05}{2}$$

$$0 \le T \le 1200 \quad (6)$$

In this equation, $E_{frp,T}$ and $F_{frp,20°C}$ are the elasticity modulus of FRP at temperature T and the elasticity modulus of FRP at 20 °C. $k_{frp,E}$ is the elastic modulus reduction factor of FRP according to temperature.

3.2 Debonding Temperature of FRP

FRP becomes bonded by attaching it to the bottom surface of the concrete using an adhesive. The performance of the adhesive affects the force transfer from the concrete to the FRP. Fig. 5 shows the changes in the strength and elastic modulus of the adhesive with the temperature (Borchert and Zilch, 2005). The closer the temperature of the adhesive is to the glass-transition temperature T_g, the lower the strength and elastic modulus of the adhesive. When the adhesive reaches the glass-transition temperature, the adhesive properties deteriorate according to the temperature, causing slip between the FRP and concrete and ultimately debonding the FRP. Therefore, it is assumed that when the temperature between the FRP and the concrete reaches the glass-transition temperature of the adhesive, the FRP debonds and does not contribute to the load-carrying capacity of the member (Camata et al., 2007; Ahmed and Kodur, 2011a).

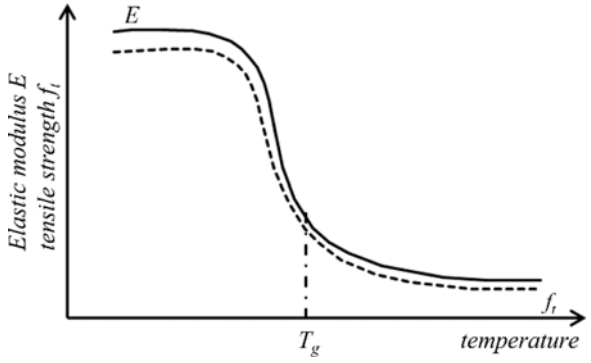

Fig. 5. Elastic Modulus and Tensile Strength of Adhesives According to the Temperature[16]

3.3 Moment Capacity Calculation Based on Section Equilibrium Analysis

After obtaining the temperature of the element through heat transfer analysis, it is possible to obtain the reduction factor for each element and whether the FRP is debonding according to the temperature. The moment capacity of FSRB can be calculated by the cross-sectional equilibrium analysis method in two cases depending on whether or not FRP debonding is performed.

3.3.1 Before the Debonding of FRP

According to the design standard ACI 440.2R-08 (2008), the moment capacity of the beam before the debonding of the FRP can be derived through the temperature, reduction factor and mechanical properties of each mesh divided by $K \times L$.

The tensile force of the beam before the debonding of the FRP is the sum of the forces acting on the mesh of each FRP and rebar. This can be derived as follows:

$$F_T = F_s + F_{frp}, \quad (7)$$

$$F_s = \sum_{i=1}^{K}\sum_{j=1}^{L} k_{s_{ij}} f_y A_{s_{ij}}, \quad (8)$$

$$F_{frp} = \sum_{i=1}^{K}\sum_{j=1}^{L} k_{frp_{ij}} f_{frp_{ij}} \Delta x_f \Delta y_f \varepsilon_{ij}. \quad (9)$$

The compressive force of the beam before the debonding of the FRP can be calculated as the sum of the forces acting on the concrete mesh (Fig. 6).

$$F_c = \sum_{i=1}^{K}\sum_{j=1}^{\frac{\beta_1 c}{\Delta y_c}} k_{c_{ij}} f_{ck} \Delta x_c \Delta y_c \quad (10)$$

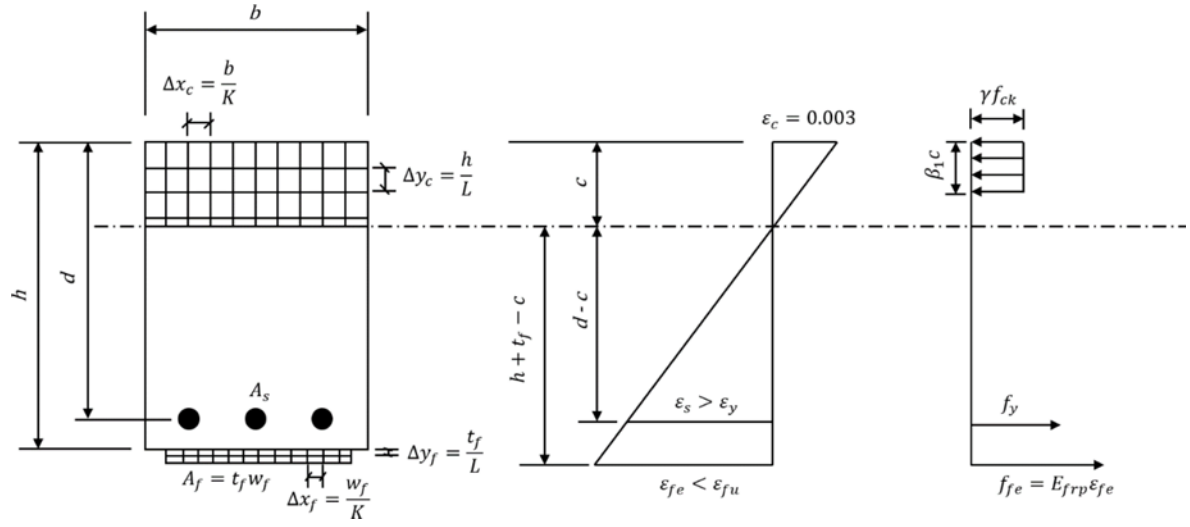

Fig. 6. Strains and Internal Forces of the Beam before the Debonding of the FRP

According to the section equilibrium analysis method, in a state of static equilibrium, Eqs. (7) and (10) must be equal. If they are not equal, the value of $\beta_1 c$ is gradually increased and the calculation is repeated. When the force of the beam is in a state of equilibrium, the moment capacity of the beam before the debonding of the FRP can be calculated as follows:

$$M_u = \sum_{i=1}^{K}\sum_{j=1}^{L} k_{s_{ij}} f_y A_{s_{ij}}\left(d - \frac{\beta_1 c}{2}\right)$$

$$+0.85\sum_{i=1}^{K}\sum_{j=1}^{L} k_{frp_{ij}} E_{frp_{ij}} \Delta x_f \Delta y_f \varepsilon_{ij}\left(h + \frac{\Delta y_f}{2} + j\Delta y_f - \frac{\beta_1 c}{2}\right). \quad (11)$$

Here, f_{ck} is the concrete compressive strength at 20s, f_y is the rebar tensile strength at 20s, E_{frp} is the elastic modulus of FRP, ε_{ij} is the strain of FRP at each mesh temperature, F_T is the total tensile force of the beam, F_s is the tensile force of the rebar, and F_c is the total compressive force of the beam. In addition, $k_{c_{ij}}$, $k_{s_{ij}}$ and $k_{frp_{ij}}$ are the reduction factors of the material for each corresponding mesh.

3.3.2 After the Debonding of the FRP

According to Erdem (2015), the moment capacity of the beam after the debonding of the FRP can be calculated through the temperature, reduction factor and mechanical properties of each mesh divided by $K \times L$.

The tensile force of the beam after the debonding of the FRP can be determined as follows (Fig. 7):

$$F_s = \sum_{i=1}^{K}\sum_{j=1}^{L} k_{s_{ij}} f_y A_{s_{ij}}. \quad (12)$$

The compressive force of the beam after the debonding of the FRP can be calculated as follows (Fig. 7):

$$F_c = \sum_{i=1}^{K}\sum_{j=1}^{\frac{\beta_1 c}{\Delta y_c}} k_{c_{ij}} f_{ck} \Delta x_c \Delta y_c. \quad (13)$$

Likewise, for the calculation of the moment capacity of the beam before the debonding of the FRP, if the beam is in a state of static equilibrium, Eqs. (12) and (13) must be equal. If not, the value of a is gradually increased and the calculation is repeated until a state of static equilibrium is reached. When the force of

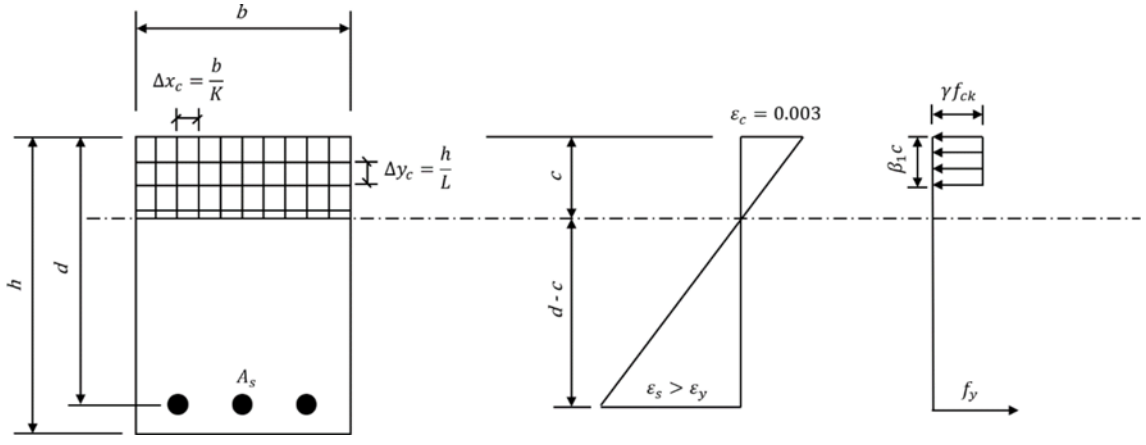

Fig. 7. Strains and Internal Forces of the Beam after the Debonding of the FRP

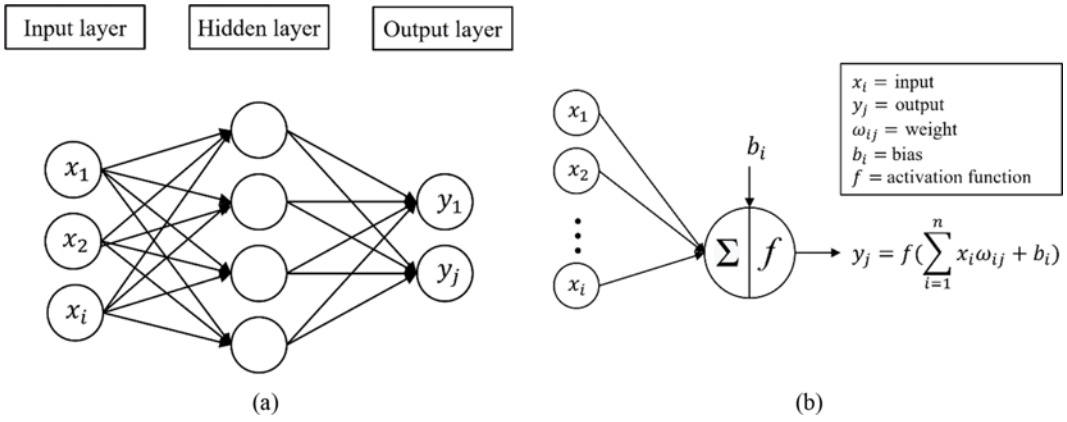

Fig. 8. The System of an Artificial Neural Networks

the beam reaches the static equilibrium state, the moment capacity of the beam before the debonding of the FRP can be calculated as follows:

$$M_u = 0.85\sum_{i=1}^{K}\sum_{j=1}^{\frac{\beta_1 c}{\Delta y_c}} k_{c_{ij}} f_{ck}\Delta x_c \Delta y_c\left(d-\frac{\Delta y_c}{2}-j\Delta y\right). \quad (14)$$

4. Artificial Neural Network

An ANN is a type of artificial intelligence technology that mimics the information processing format of the human brain (Kotsovou et al., 2017). An ANN consists of layers of neurons, including the input, output, and hidden layer types (Fig. 8(a)). The input layer is composed of several nodes that receive input data x_i with independent parameters. The output layer includes several nodes representing the prediction result y_j of the network. The hidden layer performs the main mathematical calculations on the input data x_i between the input and output layers. In the hidden layer, the input data x_i is multiplied by the assigned weight ω_{ij} and the sum of that and the bias b_i is computed. The computed value is then passed to the activation function f to represent the predicted output y_j. The weights are gradually adjusted to minimize the error between the predicted output and the target output (Haido, 2022; Thai, 2022) (Fig. 8(b)).

Various algorithms are used to minimize the error of the ANN model. However, the Levenberg-Marquardt (LM) algorithm and the Bayesian regularization (BR) algorithm are mainly used to train the ANN due to their advantages and popularity (Tran and Kim, 2022).

4.1 Levenberg–Marquardt (LM) Algorithm

The Levenberg-Marquardt (LM) algorithm is the most common method for optimizing the weights and biases among standard backpropagation (BP) algorithms. This algorithm is designed to speed up training without computing the Hessian matrix.

If the performance function has the form of a sum of squares, the Hessian matrix is approximated as shown below, and the slope can be calculated as follows (Marquardt, 1963):

$$H = J^T J, \quad (15)$$

$$g = J^T e. \quad (16)$$

Here, J is the Jacobian matrix with the first derivative of the neural network error for the weights and biases, and e is the neural network error vector.

The LM algorithm uses an approximation of the Hessian matrix in the next update, similar to Newton's method.

$$x_{k+1} = x_k - (J^T J - \mu I)^{-1} J^T e \quad (17)$$

In this equation, x is the connection weight and μ is a constant. μ decreases as the performance function decreases and increases as the performance function increases. As a result, the performance function always decreases with each iteration.

4.2 Bayesian Regularization (BR) Algorithm

The Bayesian regularization (BR) algorithm computes the weights and biases according to the LM optimization algorithm. Based on the error between the predicted output and the actual output, the weights of all nodes are adjusted to minimize the error. This algorithm adjusts the objective function by adopting Bayesian regularization and adding the mean of the sum of squares of the network connection weights to the objective function. The BR algorithm can overcome the disadvantages of the standard BP algorithm, which tends to fall into the local minimum owing to its slow convergence speed (Sun et al., 2017; Wu et al., 2022).

The objective function of the BR algorithm is expressed as follows,

$$F = \alpha E_W + \beta E_D, \quad (18)$$

where E_W is the sum of the squared network weights, E_D is the sum of the squared network errors, and α and β are the corresponding objective function parameters.

5. ANN Model for the Moment Capacity of FSRBs Exposed to Fire

5.1 Input and Output Parameters

The data consist of eight input parameters (Fig. 9): the beam width (b), beam height (h), FRP area (A_{frp}), rebar area (A_s), concrete

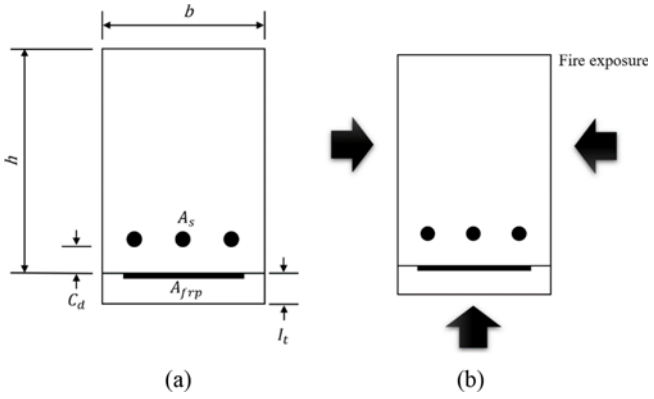

Fig. 9. Details of the Input Parameters and Conditions for the Heat Transfer Analysis: (a) Beam Cross-Section, (b) Boundary Condition

compressive strength (f_{ck}), insulation thickness (I_g), concrete cover depth (C_d), and fire exposure time (t). The output parameter used here is the moment capacity (M_u).

The temperature distribution of the beam section is determined through the heat transfer analysis verified in Chapter 2, and 400 datasets are obtained using the moment capacity calculation method in Chapter 3. The values of the input parameters are b (254-508 mm), h (304-406 mm), A_{frp} (203-406-457 mm^2), A_s (380.1-859.5-1161.3 mm^2), f_{ck} (28-40-52 MPa), I_g (25-45 mm), C_d (20-25-35-45 mm), and t (0-5-10-20-30-40-50-60-70-80-90-100-110-120-130-140-150-160-170-180 min). The tensile strength of the rebar (f_y), the elastic modulus of the FRP (E_{frp}), and the glass-transition temperature of the adhesive (T_g) were set to 400 MPa, 24000 MPa, and 87 °C, respectively.

5.2 Performance Criteria

The performance of the model is evaluated by the coefficient of determination (R^2), the mean square error (MSE), and the mean relative error ($\bar{e}$). The expressions of these three performance indicators are given below.

$$R^2 = 1 - \frac{\sum_{i=1}^{n}(\hat{y}_i - y_i)^2}{\sum_{i=1}^{n}(\hat{y}_i - \bar{y}_i)^2} \tag{19}$$

$$MSE = \frac{1}{n}\sum_{i=1}^{n}(\hat{y}_i - y_i)^2 \tag{20}$$

$$\bar{e} = \frac{1}{n}\sum_{i=1}^{n}\frac{|\hat{y}_i - y_i|}{y_i} \times 100\% \tag{21}$$

In these equations, $\hat{y}_i$ is the target value and y_i is the output value.

5.3 Determining the Hyperparameters of a Neural Network

It is essential to determine the hyperparameters of the neural network that predict the moment capacity of an FSRB exposed to fire. The key to ANN modeling is to apply appropriate hyperparameters, such as the number of hidden layers, the number of neurons in the hidden layers, and the type of algorithm. Most issues in civil engineering can be predicted well even with a single hidden layer (Naderpour et al., 2010; Nikbin et al., 2017). Therefore, a single hidden layer is also adopted in this study. In addition, TANSIG and PURELIN are used as activation functions, and the mean square error (MSE) function is selected as the measure of the ANN training approximation (Tran et al., 2019; Hosseinpour et al., 2020; Tran and Kim, 2022). In this study, the ANN model was trained by applying the LM algorithm and the BR algorithm from among many types of algorithms. The combination of these two algorithms and the number of hidden neurons can serve to determine the optimal ANN model. Here, the number of hidden neurons ranges from 1 to 20. The LM algorithm is trained and tested by randomly dividing the 400 datasets as follows: 70% for training, 15% for validation, and 15% for testing. The BR algorithm automatically controls the

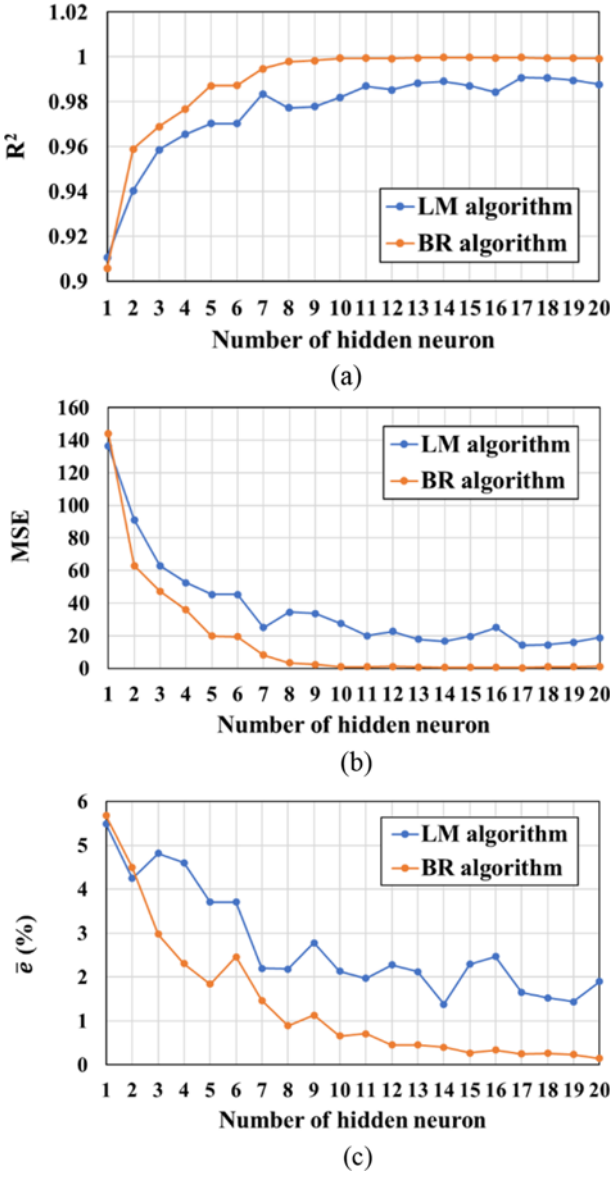

Fig. 10. Performance according to the Algorithm Type and Number of Hidden Neurons: (a) Coefficient of Determination (R^2), (b) Mean Squared Error (MSE), (c) Mean Relative Error ($\bar{e}$)

structural complexity, eliminating the need for separate training and validation sets (Tien Bui et al., 2012). The training phase is performed with all training data. Therefore, the BR algorithm develops the model by randomly dividing the 400 datasets: 70% for training and 30% for testing. Fig. 10 shows the performance of the model according to the type of algorithm and the number of hidden neurons. The hyperparameters of a neural network have a significant impact on the performance of the model. As the number of hidden neurons increases, the ability to solve complex problems improves, which in turn improves the performance of the model. Also, the BR algorithm outperforms the LM algorithm overall regardless of the number of hidden neurons. For the BR algorithm, with ten or more hidden neurons, it can be confirmed that R^2 is 0.999 or more, *MSE* is 1 or less, and $\bar{e}$ is 1% or less. For the model to which the LM algorithm is applied, the number of hidden neurons that results in the best performance is 17, and the performance indicators R^2, *MSE*, and $\bar{e}$ for the model are correspondingly 0.9908, 14.1075, and 1.6469. In the model to which the BR algorithm is applied, the number of hidden neurons resulting in the best performance is 17, while R^2, *MSE*, and $\bar{e}$ are 0.9998, 0.3338, and 0.2512%, respectively.

6. ANN Model Analysis Results

After training and testing with the 400 datasets and the hyperparameters of the neural network, the ANN model is developed to predict the moment capacity of FSRBs exposed to fire. According to the performance criteria, the ANN model is developed with the BR algorithm and 17 neurons. The MSE values for the training and testing phases were 0.9058 and 0.0886, respectively. The MSE value for all data is 0.3338. These results indicate that the ANN model worked well (Cai et al., 2019). Fig. 11 shows the relationship between the target value determined by the calculation process in Chapters 2 and 3 and the moment capacity predicted by the developed ANN model. The coefficient of determination (R^2) values during the training and testing steps are 0.9999 and 0.9995, respectively. The coefficient of determination (R^2) for all 400 datasets is 0.9995. These results suggest that the ANN model has high generalization ability (Cai et al., 2019). Fig. 12(a) shows the results of a comparison between the output and target values of the developed ANN model. The maximum

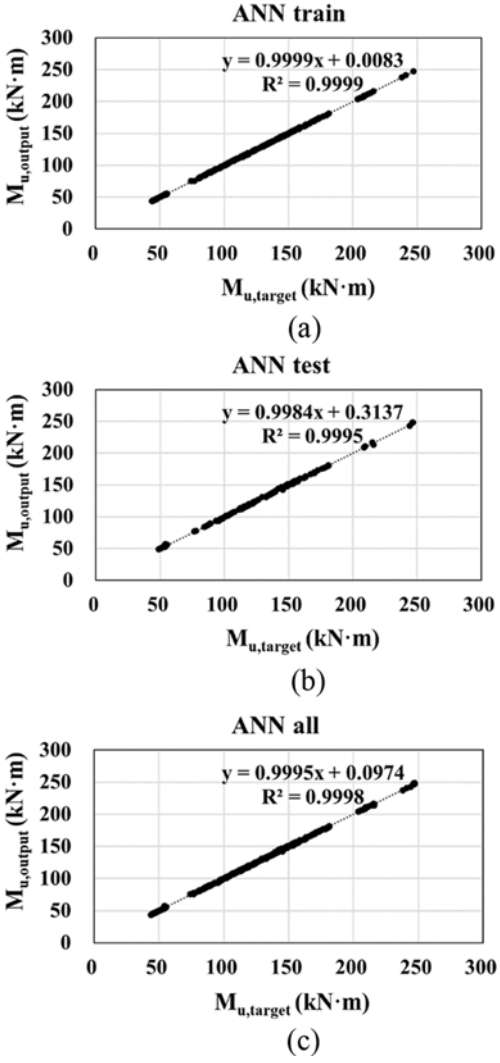

Fig. 11. Comparison of the Calculated Target and Predicted Output Moment Capacity: (a) Train, (b) Test, (c) All

error between the output value and the target value is 3.04 kN·m, and the average error for the 400 datasets is 0.35 kN·m. The relative error (e) of the output value and the target value is shown in Fig. 12(b). The expression of the relative error (e) is identical to that in Eq. (22). The maximum relative error (e) is 5.32%, but

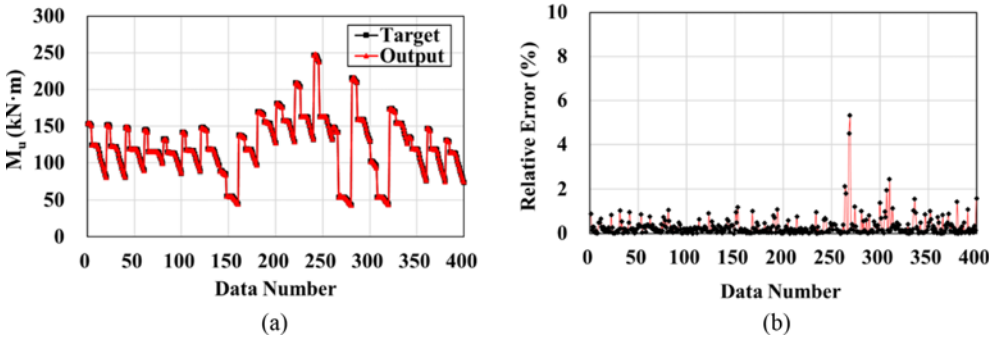

Fig. 12. Evaluating the Computational Accuracy of ANN Model: (a) Target and Output Moment Capacity, (b) Relative Error of the Moment Capacity

Table 1. Calculated Target and Predicted Output Moment Capacities

No.	b (mm)	h (mm)	A_{frp} (mm^2)	A_s (mm^2)	f_{ck} (MPa)	I_t (mm)	C_d (mm)	t (min)	$M_{u,target}$ (kN·m)	$M_{u,output}$ (kN·m)	e (%)
1	254	406	203	859.5	52	25	20	0	153.07	154.43	0.88
2	254	406	203	859.5	52	25	20	5	153.93	153.70	0.15
3	254	406	203	859.5	52	25	20	10	153.23	153.69	0.30
4	254	406	203	859.5	52	25	20	20	151.01	151.45	0.29
5	254	406	203	859.5	52	25	20	30	124.28	124.25	0.03
6	254	406	203	859.5	52	25	20	40	124.28	124.13	0.13
7	254	406	203	859.5	52	25	20	50	124.11	124.09	0.02
8	254	406	203	859.5	52	25	20	60	124.11	124.14	0.03
9	254	406	203	859.5	52	25	20	70	123.94	124.55	0.49
10	254	406	203	859.5	52	25	20	80	123.94	124.54	0.48
11	254	406	203	859.5	52	25	20	90	123.94	123.11	0.68
12	254	406	203	859.5	52	25	20	100	118.85	119.20	0.30
13	254	406	203	859.5	52	25	20	110	113.16	113.34	0.16
14	254	406	203	859.5	52	25	20	120	107.79	107.49	0.28
15	254	406	203	859.5	52	25	20	130	102.73	102.65	0.08
16	254	406	203	859.5	52	25	20	140	98.11	98.27	0.16
17	254	406	203	859.5	52	25	20	150	93.64	93.77	0.14
18	254	406	203	859.5	52	25	20	160	89.42	89.30	0.13
19	254	406	203	859.5	52	25	20	170	85.42	85.20	0.26
20	254	406	203	859.5	52	25	20	180	81.64	81.58	0.07
.	.	.	.	.	.	.	.	.	.	.	.
.	.	.	.	.	.	.	.	.	.	.	.
.	.	.	.	.	.	.	.	.	.	.	.
361	254	304	406	859.5	52	25	20	0	146.99	147.72	0.50
362	254	304	406	859.5	52	25	20	5	146.70	146.71	0.01
363	254	304	406	859.5	52	25	20	10	146.04	146.30	0.18
364	254	304	406	859.5	52	25	20	20	143.92	143.92	0.00
365	254	304	406	859.5	52	25	20	30	119.13	120.12	0.83
366	254	304	406	859.5	52	25	20	40	119.13	119.15	0.02
367	254	304	406	859.5	52	25	20	50	118.95	119.06	0.08
368	254	304	406	859.5	52	25	20	60	118.95	118.53	0.35
369	254	304	406	859.5	52	25	20	70	118.78	119.08	0.25
370	254	304	406	859.5	52	25	20	80	118.78	119.37	0.49
371	254	304	406	859.5	52	25	20	90	118.61	117.56	0.89
372	254	304	406	859.5	52	25	20	100	112.67	113.10	0.38
373	254	304	406	859.5	52	25	20	110	107.13	107.26	0.12
374	254	304	406	859.5	52	25	20	120	102.05	101.62	0.42
375	254	304	406	859.5	52	25	20	130	97.14	96.84	0.31
376	254	304	406	859.5	52	25	20	140	92.53	92.62	0.09
377	254	304	406	859.5	52	25	20	150	88.21	88.42	0.24
378	254	304	406	859.5	52	25	20	160	84.14	84.13	0.01
379	254	304	406	859.5	52	25	20	170	80.30	80.20	0.12
380	254	304	406	859.5	28	25	20	180	76.66	75.57	1.44
381	254	304	406	859.5	28	25	20	0	130.92	130.92	0.00
382	254	304	406	859.5	28	25	20	5	130.74	130.53	0.16
383	254	304	406	859.5	28	25	20	10	130.33	130.56	0.18
384	254	304	406	859.5	28	25	20	20	129.00	129.02	0.02
385	254	304	406	859.5	28	25	20	30	114.49	114.13	0.31
386	254	304	406	859.5	28	25	20	40	114.31	114.24	0.07
387	254	304	406	859.5	28	25	20	50	114.14	114.69	0.48
388	254	304	406	859.5	28	25	20	60	113.97	114.01	0.03
389	254	304	406	859.5	28	25	20	70	113.80	113.71	0.08
390	254	304	406	859.5	28	25	20	80	113.63	113.73	0.09
391	254	304	406	859.5	28	25	20	90	113.29	112.08	1.08
392	254	304	406	859.5	28	25	20	100	107.79	108.02	0.21
393	254	304	406	859.5	28	25	20	110	102.80	102.79	0.01
394	254	304	406	859.5	28	25	20	120	97.94	97.80	0.14
395	254	304	406	859.5	28	25	20	130	93.37	93.47	0.11
396	254	304	406	859.5	28	25	20	140	89.21	89.40	0.22
397	254	304	406	859.5	28	25	20	150	85.17	85.22	0.05
398	254	304	406	859.5	28	25	20	160	81.37	81.08	0.35
399	254	304	406	859.5	28	25	20	170	77.77	77.66	0.14
400	254	304	406	859.5	28	25	20	180	74.37	75.57	1.60

the average relative error value ($\bar{e}$) of the 400 datasets is 0.2512%, which is less than 1% of the maximum. Table 1 shows the input, output, target value, and relative error of the 400 datasets. Through the average difference between the output value and the target value and the average relative error value, it was confirmed that the ANN model has high computational accuracy. Therefore, the ANN model presented here can be used to predict the moment capacity of FSRBs exposed to fire.

$$e = \text{Relative Error} = \frac{|\hat{y}_i - y_i|}{y_i} \times 100\% \quad (22)$$

Here, $\hat{y}_i$ is the target value and y_i is the output value.

7. Parametric Study Using the ANN Model

The developed ANN model with high computational accuracy and good generalization ability is used to evaluate the effects of several input parameters on the moment capacity. The effects of each of these input parameters on the moment capacity are described below.

7.1 Effect of the Reinforcement Area A_s on M_u

The effect of the rebar area (A_s) on the moment capacity is studied using the ANN model. The input parameters are $b = 254$ mm, $h = 406$ mm, $A_{frp} = 203$ mm^2, $A_s = 380.1$, 859.5, 1161.2 mm^2, $f_{ck} = 28$ MPa, $I_t = 45$ mm, $C_d = 25$ mm, and $t = 0$, 5, 10, 20, 30, 40, 50, 60, 70, 80, 90, 100, 110, 120, 130, 140, 150, 160, 170, 180 min. The effect of the rebar area on the moment is shown in Fig. 13(a). The moment capacity clearly decreased as the fire exposure time increased, but the moment capacity increased as the rebar area increased.

7.2 Effect of the Concrete Cover Depth C_d on M_u

The effect of the concrete cover depth (C_d) on the moment capacity is also studied using the ANN model. The input parameters are $b = 254$ mm, $h = 406$ mm, $A_{frp} = 203$ mm^2, $A_s = 859.5$ mm^2, $f_{ck} = 52$ MPa, $I_t = 25$ mm, $C_d = 20$, 30, 40 mm, and $t = 0$, 5, 10, 20, 30, 40, 50, 60, 70, 80, 90, 100, 110, 120, 130, 140, 150, 160, 170, 180 min. The effect of the concrete cover depth is illustrated in Fig. 13(b). For a short fire time, a smaller concrete cover depth acts favorably on the moment capacity, but for a long fire time, a decrease in the concrete cover depth has an adverse effect on the moment capacity. For a fire exposure time of 100 minutes or more, it is confirmed that as the concrete cover depth becomes shallower, the tensile strength of the rebar decreases rapidly due to the high temperature, which affects the moment capacity.

7.3 Effect of the FRP Area A_{frp} on M_u

The effect of the FRP area (A_{frp}) on the moment capacity was subsequently studied using the ANN model. The input parameters are $b = 508$ mm, $h = 406$ mm, $A_{frp} = 203$, 406, 457 mm^2, $A_s = 1161.3$ mm^2, $f_{ck} = 28$ MPa, $I_t = 45$ mm, $C_d = 35$ mm, and $t = 0$, 5, 10, 20, 30, 40, 50, 60, 70, 80, 90, 100, 110, 120, 130, 140, 150, 160, 170, 180 min. As shown in Fig. 13(c), while the FRP area affects the moment capacity for a short fire time, the effect on the moment capacity as the fire time increases is negligible. When the fire exposure time exceeds 50 minutes, the debonding of the FRP occurs, and the FRP area does not affect the moment capacity

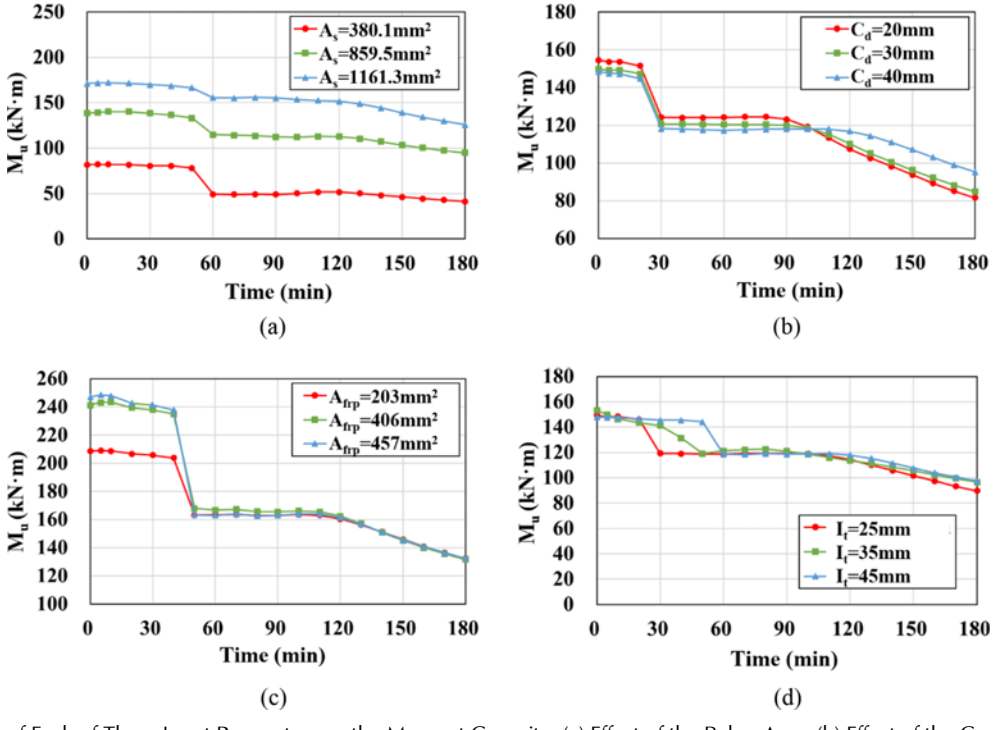

Fig. 13. The Effects of Each of These Input Parameters on the Moment Capacity: (a) Effect of the Rebar Area, (b) Effect of the Cover Depth, (c) Effect of the FRP Area, (d) Effect of the Insulation Thickness

of the beam. That is, when the adhesive temperature between the FRP and concrete exceeds the glass-transition temperature (T_g), the FRP is debonded and the FRP area does not affect the moment capacity.

7.4 Effect of the Insulation Thickness I_t on M_u

The ANN model is used to study the effect of the insulation thickness I_t on the moment capacity. The input parameters are b = 254 mm, h = 406 mm, A_{frp} = 203 mm^2, As = 859.5 mm^2, f_{ck} = 52 MPa, I_t = 25, 35, 45 mm, C_d = 35 mm, and t = 0, 5, 10, 20, 30, 40, 50, 60, 70, 80, 90, 100, 110, 120, 130, 140, 150, 160, 170, 180 min. Fig. 13(d) shows the effect of the insulation thickness on the moment capacity. Although the insulation thickness has no effect at short fire exposure times, an increase in the insulation thickness may delay the point at which the debonding of the FRP occurs. When the insulation thickness increases from 25 mm to 45 mm, the debonding time of the FRP increases from 30 minutes to 60 minutes. In addition, the insulation thickness for a long fire exposure time prevents a sharp decrease in the tensile strength of the rebar, which affects the moment capacity.

8. Conclusions

In this study, the validity of a heat transfer analysis using ABAQUS is verified based on Ahmed's experimental and analysis results and a formula for calculating moment capacity of FSRBs exposed to fire is established. Furthermore, a heat transfer analysis is conducted using the FRP area, the rebar area, the concrete compressive strength, the insulation thickness, the concrete cover thickness, and the fire exposure time as variables, and 400 moment capacity values according to each variable are calculated with the formula. An ANN model is developed to calculate the moment capacity of a FSRB exposed to fire through a sensitivity study using the type of algorithm and the number of neurons in the hidden layers as variables. Using the developed ANN model, the effects of the rebar area, concrete cover depth, FRP area, insulation thickness and fire exposure time on the moment capacity are investigated. Through the ANN model, it is possible to predict the moment capacity of a FSRB exposed to fire quickly and effectively. The conclusions of this study are given below.

1. The ANN model trained by the BR algorithm rather than the LM algorithm is more accurate for predicting the moment capacity of a FSRB exposed to fire, and using 17 hidden neurons is effective in terms of the performance outcome.
2. The coefficient of determination, the average error, and the average relative error of the developed ANN model are 0.9995, 0.35, and 0.2512%, respectively, all of which have high generalization ability and good computational accuracy.
3. The moment capacity increases as the rebar area increases and decreases as the fire exposure time increases.
4. For a short fire exposure time, the moment capacity increases as the concrete cover depth decreases, but after a certain point, a decrease in the concrete cover depth causes a sharp decrease in the moment capacity.
5. The FRP area affects the moment capacity during the fire exposure time before the FRP is debonded, but the effect becomes negligible after the debonding.
6. For a short fire exposure time, the insulation thickness affects the moment capacity by delaying the time of FRP debonding, and during the subsequent fire exposure time, the insulation thickness prevents a sudden decrease in the tensile strength of the rebar, which affects the moment capacity.

Acknowledgments

This research was supported by Korea Electric Power Corporation (Grant number: R21XO01-33).

ORCID

Seong-Muk Kang https://orcid.org/0009-0008-0124-6180
Jin-Kook Kim https://orcid.org/0000-0001-6857-7824

References

ABAQUS (2010) Abaqus 6.10: analysis user's manual. Dassault Systemes Simulia Corp: Providence, RI

ACI 440.2R-08 (2008) ACI 440.2R-08: Guide for the design and construction of externally bonded FRP systems for strengthening concrete structures. American Concrete Institute, Farmington Hills

ASTM E 119-11 (2010) Standard methods of fre tests of building construction and materials, West Conshohocken, PA, USA

Ahmed A, Kodur VKR (2011a) Effect of bond degradation on fire resistance of FRP-strengthened reinforced concrete beams. *Composites Part B: Engineering* 42.2:226-237, DOI: 10.1016/j.compositesb.2010.11.004

Ahmed A, Kodur VKR (2011b) The experimental behavior of FRP-strengthened RC beams subjected to design fire exposure. *Engineering Structures* 33(7):2201-2211, DOI: 10.1016/j.engstruct.2011.03.010

Bisby LA (2003) Fire behaviour of fibre-reinforced polymer (FRP) reinforced or confined concrete. PhD Thesis, Queen's University at Kingston, Canada

Bengar HA, Abdollahtabar M, Shayanfar J (2016) Predicting the ductility of RC beams using nonlinear regression and ANN. *Iranian Journal of Science and Technology, Transactions of Civil Engineering* 40(4): 297-310, DOI: 10.1007/s40996-016-0033-0

Bakis CE, Bank LC, Brown V, Cosenza E, Davalos J, Lesko J, Machida A, Rizkalla S, Triantafillou T (2002) Fiber-reinforced polymer composites for construction—state-of-the-art review. *Journal of composites for construction* 6(2):73-87, DOI: 10.1061/(ASCE)1090-0268(2002)6:2(73)

Bergman T, Incropera F, Lavine A, DeWitt D (2011) Introduction to heat transfer. Wiley, Hoboken

Borchert K, Zilch K (2005) Time depending thermo mechanical bond behavior of epoxy bonded pre-stressed FRP-reinforcement. *Special Publication* 230:671-684

Camata G, Pasquini F, Spacone E (2007) High Temperature Flexural Strengthening with Externally Bonded FRP Reinforcement. In: Proceedings of 8th International Symposium on Fiber Reinforced Polymer (FRP) Reinforcement for Concrete Structures (FRP8RCS):1-

10
Cai B, Xu L-F, Fu F (2019) Shear resistance prediction of postfre reinforced concrete beams using artifcial neural network. *International Journal of Concrete Structures and Materials* 13(1):46, DOI: 10.1186/s40069-019-0358-8
Eurocode 2 (2004) Design of concrete structures - Part 1-1: General rules and rules for buildings. European Committee for Standardization (CEN) London, UK
Eurocode 4 (2005) Design of composite steel and concrete structures - Part 1-2: General Rules-Structural Fire Design. European Committee for Standardization (CEN) London, UK
Erdem H (2010) Prediction of moment capacity of reinforced concrete slabs in fire using artificial neural networks. *Advances in Engineering Software* 41(2):270-276, DOI: 10.1016/j.advengsoft.2009.07.006
Erdem H (2015) Predicting the moment capacity of RC beams exposed to fire using ANNs. *Construction and Building Materials* 101(Part 1):30-38 DOI: 10.1016/j.conbuildmat.2015.10.049
Haido JH (2022) Prediction of the shear strength of RC beam-column joints using new ANN formulations. *Structures* 38:1191-1209, DOI: 10.1016/j.istruc.2022.02.046
Hawileh RA, Naser M, Zaidan W, Rasheed HA (2009) Modeling of insulated CFRP-strengthened reinforced concrete T-beam exposed to fire. *Engineering Structures* 31(12):3072-3079, DOI: 10.1016/j.engstruct.2009.08.008
Hosseinpour M, Sharif Y, Sharif H (2020) Neural network application for distortional buckling capacity assessment of castellated steel beams. *Structures* 27:1174-1183, DOI: 10.1016/j.istruc.2020.07.027
Kodur VKR, Bhatt PP (2018) A numerical approach for modeling response of fiber reinforced polymer strengthened concrete slabs exposed to fire. *Composite Structures* 187:226-240, DOI: 10.1016/j.compstruct.2017.12.051
Kotsovou GM, Cotsovos DM, Lagaros ND (2017) Assessment of RC exterior beam-column joints based on artificial neural networks and other methods. *Engineering Structures* 144:1-18, DOI: 10.1016/j.engstruct.2017.04.048
Marquardt DW (1963) An algorithm for least-squares estimation of nonlinear parameters. *Journal of the Society for Industrial and Applied Mathematics* 11.2:431-441
Naser M, Abu-Lebdeh G, Hawileh R (2012) Analysis of RC T-beams strengthened with CFRP plates under fire loading using ANN. *Construction and Building Materials* 101(Part 1):30-38, DOI: 10.1016/j.conbuildmat.2012.07.001
Naderpour H, Kheyroddin A, Amiri G G (2010) Prediction of FRP-confined compressive strength of concrete using artificial neural networks. *Composite Structures* 92(12):2817-2829, DOI: 10.1016/j.compstruct.2010.04.008
Nikbin MI, Rahimi RS, Allahyari H (2017) A new empirical formula for prediction of fracture energy of concrete based on the artifcial neural network. *Engineering Fracture Mechanics* 186:466-482, DOI: 10.1016/j.engfracmech.2017.11.010
Panahi M, Zareei SA, Izadi A (2021) Flexural strengthening of reinforced concrete beams through externally bonded FRP sheets and near surface mounted FRP bars. *Case Studies in Construction Materials* 15:e00601, DOI: 10.1016/j.cscm.2021.e00601
Sun Z, Chen Y, Li X, Qin X, Wang H (2017) A bayesian regularized artificial neural network for adaptive optics forecasting. *Optics Communications* 382:519-527, DOI: 10.1016/j.optcom.2016.08.035
Thai H-T (2022) Machine learning for structural engineering: a state-of-the-art review. *Structures* 38:448-491, DOI: 10.1016/j.istruc.2022.02.003
Tran VL, Kim JK(2022) Revealing the nonlinear behavior of steel flush endplate connections using ANN-based hybrid models. *Journal of Building Engineering* 57:104878, DOI: 10.1016/j.jobe.2022.104878
Tien Bui D, Pradhan B, Lofman O, Revhaug I, Dick OB (2012) Landslide susceptibility assessment in the hoa binh province of vietnam: A comparison of the levenbergmarquardt and bayesian regularized neural networks. *Geomorphology* 171-172:12-29, DOI: 10.1016/j.geomorph.2012.04.023
Tran V, Thai D, Kim S (2019) Application of ANN in predicting ACC of SCFST column. *Composite Structures* 228:111332, DOI: 10.1016/j.compstruct.2019.111332
Wu D, Huang H, Qiu S, Liu Y, Wu Y, Ren Y, Mou J (2022) Application of Bayesian regularization back propagation neural network in sensorless measurement of pump operational state. *Energy Reports* 8:3041-3050, DOI: 10.1016/j.egyr.2022.02.072
Xiang K, Wang GH (2013) Calculation of flexural strengthening of fire-damaged reinforced concrete beams with CFRP sheets. *Procedia Engineering* 52:446-452, DOI: 10.1016/j.proeng.2013.02.167